MYU Tokyo

S & M 4094

Piezoelectric Nanogenerator Based on Vertically Aligned ZnO Nanowire Arrays for Piezoelectric Energy Harvesting and Sensor

Ming-Cheng Kao[1*] and Kai-Huang Chen[2**]

[1]Graduate Institute of Aeronautics, Department of Information and Communication Engineering, Chaoyang University of Technology, Taichung 413310, Taiwan
[2]Department of Electronic Engineering, Cheng Shiu University, Kaohsiung 83347, Taiwan

(Received March 17, 2025; accepted May 23, 2025)

Keywords: ZnO, nanowire, piezoelectric, energy harvesting, sensor

In this study, we investigated the effects of seed layer thickness on the structural and piezoelectric properties of ZnO nanowires (ZNWs) and evaluated their energy harvesting performance. ZNWs with seed layer thicknesses of 100, 200, 300, and 400 nm were synthesized and characterized. The results show that a ZNW with a 300 nm seed layer (ZNW-300) has the highest aspect ratio, resulting in excellent piezoelectric performance with a piezoelectric charge coefficient (d_{33}) of 10.5 pm/V and a peak-to-peak voltage output of 4.6 V. The energy harvesting performance was further verified through a 150 μF capacitor charging test, which successfully charged to 3.5 V in 12 s, generating a power output of 76.56 μW. These findings highlight the potential of ZNW-based piezoelectric nanogenerators for self-powered applications, including wearable electronics, wireless sensor networks, and sustainable energy harvesting systems.

1. Introduction

In recent years, the continued growth of the global demand for energy and increasingly severe environmental problems have generated much attention on the development of renewable energy and environmentally friendly energy technologies. Among the various available approaches, piezoelectric energy harvesting has been extensively studied owing to its ability to convert ambient mechanical energy into electrical energy, offering potential solutions for powering microdevices and low-power electronics.(1–4) This energy conversion is facilitated through the piezoelectric effect, where mechanical strain induces charge displacement within specific materials, resulting in the generation of voltage and current.(5–7) Piezoelectric nanogenerators (PENGs) have been widely adopted for use in wearable electronics, wireless sensor networks, and self-powered devices because of their ability to function effectively under low-frequency mechanical vibrations.(8–12) Zinc oxide (ZnO) has been extensively employed as a key material in PENGs owing to its wide bandgap, high piezoelectric coefficient, and chemical stability.(13–15) ZnO nanowires (ZNWs) have been recognized for their large surface-area-to-volume ratio and superior piezoelectric properties.(16–18) The piezoelectric performance of

*Corresponding author: e-mail: kmc@cyut.edu.tw
**Corresponding author: e-mail: 5977@gcloud.csu.edu.tw
https://doi.org/10.18494/SAM5634

ZNWs is largely governed by their crystal structure, alignment, and dimensions, all of which are strongly affected by the seed layer on which they are grown. Seed layer thickness plays a crucial role in determining the nucleation and growth characteristics of ZNWs, making its control critical in optimizing their performance in piezoelectric applications.(19–21)

Several studies have been conducted on the effect of seed layer thickness on the growth behavior of ZNWs, including their crystallographic orientation, aspect ratio, and defect density.(22–24) However, research on the effects of different seed layer thicknesses on the piezoelectric properties of ZNWs for energy harvesting and sensor applications is still limited. Understanding the relationship between seed layer thickness and the piezoelectric properties of ZNWs is crucial for enhancing the design and fabrication of high-efficiency PENGs. In this study, we investigate the effects of ZnO seed layer thickness on the structural and piezoelectric properties of ZNWs and evaluate their energy harvesting performance. ZNWs were synthesized on seed layers with thicknesses of 100, 200, 300, and 400 nm by a hydrothermal method. The morphological and crystallographic properties of the nanowires (NWs) were characterized by scanning electron microscopy (SEM) and X-ray diffraction (XRD). The piezoelectric response was assessed through d_{33} measurements, while the energy harvesting capability was evaluated by measuring the voltage output and capacitor charging performance.

2. Materials and Methods

The ZnO seed layers were deposited on fluorine-doped tin oxide (FTO) substrates using an RF magnetron sputtering system. High-purity ZnO (99.99%) was used as the target material. The FTO substrates were cleaned ultrasonically in acetone, ethanol, and deionized water for 15 min each, followed by drying with nitrogen gas. The sputtering process was carried out under a base pressure of 5×10^{-6} Torr, with an RF power density of 7.4 W/cm^2 and an argon flow rate of 20 sccm. The substrate temperature was maintained at 200 °C during deposition. ZnO seed layers with thicknesses of 100, 200, 300, and 400 nm were prepared by varying the deposition time. The deposition process is schematically illustrated in Fig. 1(a). ZNWs were grown on the ZnO seed layers by a chemical bath deposition (CBD) method. The growth solution was prepared by dissolving zinc nitrate hexahydrate [$Zn(NO_3)_2 \cdot 6H_2O$] and hexamethylenetetramine (HMTA, $C_6H_{12}N_4$) in deionized water at a concentration of 25 mM each. The seeded FTO substrates were immersed in the growth solution and maintained at 90 °C for 6 h in a laboratory oven. After growth, the samples were thoroughly rinsed with deionized water to remove any residual salts and dried at room temperature. The growth process is depicted in Fig. 1(b). The samples were labeled ZSL-100, ZSL-200, ZSL-300, and ZSL-400 for seed layers, and ZNW-100, ZNW-200, ZNW-300, and ZNW-400 for corresponding NW growths.

The structural properties of the ZnO seed layers and NWs were characterized by XRD with Cu Kα radiation (λ = 1.5406 Å). The surface morphology and dimensions of the ZNWs were examined by field-emission SEM (FE-SEM, Hitachi SU8010). The piezoelectric coefficient (d_{33}) of the ZNWs was measured using a Quasi Static Piezo d_{33} Meter (PKD3-4000). The methodology for piezoelectric coefficient measurement is illustrated in Figs. 1(e)–1(g), where localized mechanical stress is applied using the Piezo d_{33} Meter, and the resulting piezoelectric response is

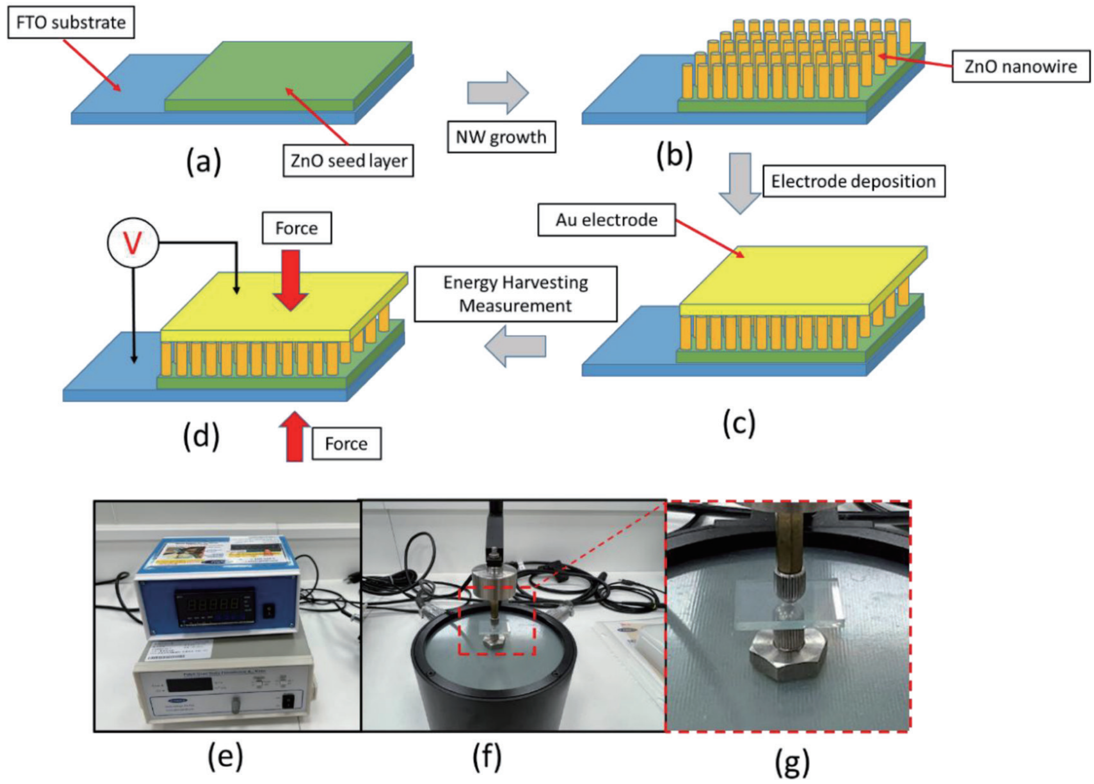

Fig. 1. (Color online) (a)–(c) Schematic of the preparation of ZNW PENGs. (d) Piezoelectric energy harvesting measurement. (e)–(g) Methodology for piezoelectric coefficient measurement.

measured and calibrated. PENGs were fabricated by sandwiching ZNW arrays between the FTO substrate and a top Au electrode. The assembly process is shown in Fig. 1(c). To evaluate the energy harvesting performance of the ZNW-based PENG, cyclic mechanical force was applied using a linear motor system, as shown in Fig. 1(d). The generated output voltage was recorded using an oscilloscope. Additionally, a capacitor charging test was performed to assess the power generation efficiency. A 150 μF capacitor was connected to the nanogenerator, and the voltage buildup over time was measured.

3. Results and Discussion

The XRD patterns of ZnO seed layers with different thicknesses (ZSL-100, ZSL-200, ZSL-300, and ZSL-400) are presented in Fig. 2. The diffraction peaks confirm the hexagonal wurtzite crystal structure of ZnO with a dominant (002) peak, indicating preferential growth along the c-axis. As the thickness of the ZnO seed layer increases from 100 to 400 nm, the intensity of the (002) peak increases significantly, indicating improved crystallinity and preferential orientation along the *c*-axis. The ZSL-400 sample exhibits the highest diffraction intensity on the (002) plane, which indicates that a thicker seed layer promotes enhanced crystal growth and grain alignment. This improvement can be attributed to a higher nucleation density, which facilitates

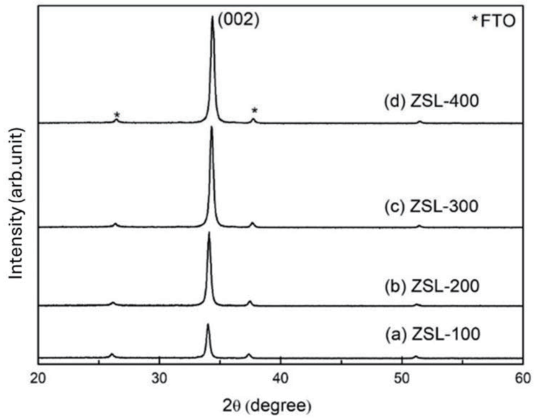

Fig. 2. XRD patterns of (a) ZSL-100, (b) ZSL-200, (c) ZSL-300, and (d) ZSL-400.

the formation of well-aligned ZnO grains. Furthermore, the full-width at half-maximum (*FWHM*) of the (002) peak decreases with increasing seed layer thickness, indicating a reduction in structural defect density and improved crystallite size.

To further analyze the shift in (002) peak position, Fig. 3 shows enlarged XRD patterns in the 33.4 to 35° range. The (002) peak positions for different seed layer thicknesses are as follows: ZSL-100 at 34.02°, ZSL-200 at 34.1°, ZSL-300 at 34.29°, and ZSL-400 at 34.38°. The observed shift in peak position with increasing seed layer thickness suggests a reduction in residual strain and an improvement in lattice ordering. The systematic increase in peak position towards higher angles indicates compressive stress relaxation within the ZnO film, contributing to enhanced crystallinity and structural stability.

Table 1 shows the structural parameters of the ZnO seed layers with different thicknesses derived from the XRD data. As observed, the (002) peak position shifts slightly to higher angles as the seed layer thickness increases, indicating reduced residual strain and enhanced crystallinity. Additionally, the *FWHM* values show a slight increase with seed layer thickness, which affects the estimated crystallite size. The crystallite size (D) of the ZnO seed layers was estimated using the Scherrer equation:[25]

$$D = \frac{K}{\lambda \cos\theta}, \tag{1}$$

where K is 0.9, λ is the X-ray wavelength (0.154 nm), β is the *FWHM* of the (002) diffraction peak, and θ is the Bragg angle. The estimated relative grain boundary densities corresponding to each seed layer thickness are shown in Table 1. The grain boundary density is estimated using the reciprocal of the crystallite size. The data indicate that the crystallite size decreases as the seed layer thickness increases, suggesting that thicker films introduce a higher density of grain boundaries. The structural integrity and crystallographic orientation of the seed layer directly affect the subsequent ZNW growth, affecting their alignment, morphology, and ultimately, the performance of PENGs. The same results are also shown in Fig. 4, which shows the plan-view SEM images of ZnO seed layers with different thicknesses. These images illustrate that as the

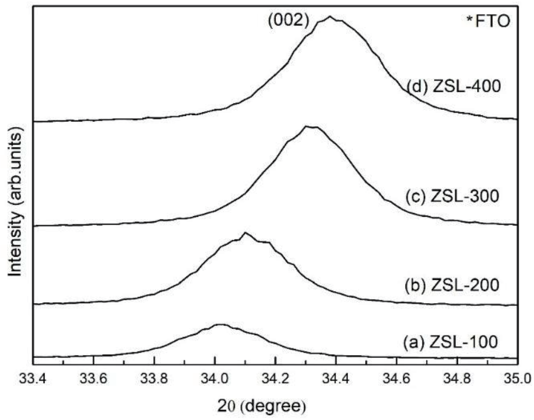

Fig. 3. Enlarged XRD patterns of (a) ZSL-100, (b) ZSL-200, (c) ZSL-300, and (d) ZSL-400 at 33.4 to 35°.

Table 1
Structured parameters of ZnO seed layers of different thicknesses obtained from XRD data.

Sample	2θ (deg)	*FWHM* (deg)	Crystallite size (nm)	Grain boundary density
ZSL-100	34.02	0.3528	23.56108	0.0424
ZSL-200	34.1	0.37252	22.3185	0.0448
ZSL-300	34.29	0.37908	21.94375	0.0456
ZSL-400	34.38	0.39366	21.13544	0.0473

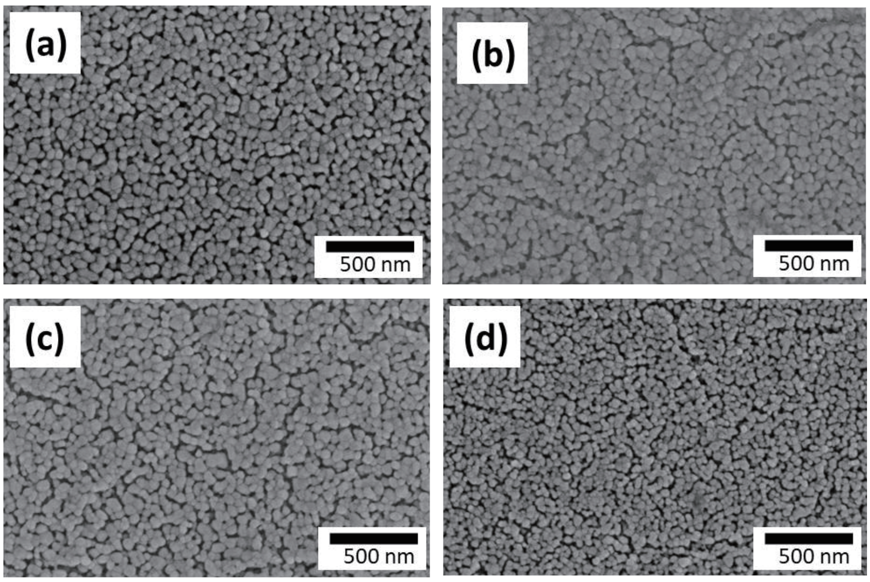

Fig. 4. Plane-view SEM images of (a) ZSL-100, (b) ZSL-200, (c) ZSL-300, and (d) ZSL-400.

seed layer thickness increases, the grains become smaller and the grain boundary density increases.

Figure 5 shows the cross-sectional SEM images of ZNWs grown on different seed layer thicknesses. Table 2 shows the structural parameters of the NWs, namely, length, diameter,

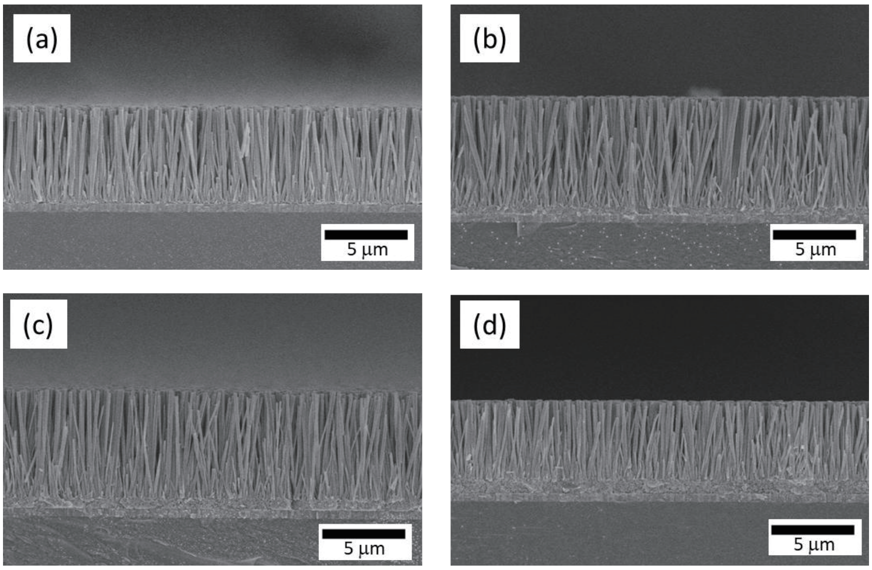

Fig. 5. Cross-sectional SEM images of (a) ZNW-100, (b) ZNW-200, (c) ZNW-300, and (d) ZNW-400.

Table 2
Structural parameters of ZNWs with different seed layer thicknesses.

Sample	Length (nm)	Diameter (nm)	Aspect ratio	d_{33}
ZNW-100	5710	150	38.07	7.5
ZNW-200	6220	130	47.85	8.3
ZNW-300	6680	110	60.72	10.5
ZNW-400	4850	100	48.50	9.2

aspect ratio, and piezoelectric coefficient (d_{33}). The results show that as the seed layer thickness increases from 100 nm (ZNW-100) to 300 nm (ZNW-300), the NW length initially increases from 5710 nm to a maximum value of 6680 nm (ZNW-300). However, further increase in seed layer thickness to 400 nm (ZNW-400) resulted in a significant reduction in length to 4850 nm. The results show that a seed layer thickness of 300 nm is optimal for achieving the maximum growth of ZNWs, which may be due to the optimal grain orientation of ZNW-300 and the excessive grain boundaries of ZNW-400 resulting in shorter NWs. In addition, the NW diameter showed a decreasing trend from 150 nm (ZNW-100) to 100 nm (ZNW-400). The decrease in diameter with increasing seed layer thickness can be attributed to the change in the nucleation process, where thicker seed layers lead to smaller grains and thus finer NWs. This phenomenon affects the aspect ratio (ratio of length to diameter), with the highest value being 56.55 for ZNW-300, indicating that this condition favors the most favorable anisotropic growth of ZNWs. The piezoelectric coefficient (d_{33}) is a key parameter for evaluating the piezoelectric properties of ZNWs, and its variation trend is similar to that of the aspect ratio. The highest d_{33} value of 10.5 pm/V was observed for ZNW-300, showing that the optimum seed layer thickness is beneficial for enhancing the piezoelectric performance. This improvement can be attributed to the increased aspect ratio, which enhances the mechanical deformation response under applied stress. In contrast, the decrease in d_{33} for ZNW-400 (9.2 pm/V) may be associated with the shorter NWs, resulting in a lower piezoelectric efficiency as a result of the decreased aspect ratio. Only ZSL-400 has no subsequent NW growth and exhibits a substantially lower piezoelectric coefficient (d_{33} = 5.6 pm/V). This phenomenon indicated that the presence of vertically aligned ZNWs significantly enhances the piezoelectric response. In addition, the optimized d_{33} value obtained in this study (10.5 pm/V) is higher than that of ZnO nanorods synthesized via chemical bath deposition, for which a d_{33} value of 7 pm/V was reported in a previous study.[26]

Figure 6 shows the working mechanism, experimental validation, and energy harvesting performance of the ZNW-based piezoelectric energy harvester. Figure 6(a) illustrates the energy harvesting circuit, where a ZNW-based piezoelectric device is connected to a bridge rectifier circuit to convert the AC piezoelectric output into DC voltage. The rectified voltage is subsequently stored in a capacitor for energy storage and potential applications in self-powered systems. Figure 6(b) shows the experimental demonstration of the device's energy harvesting capability. The left image shows the device connected to an LED, and the right image captures the moment when a user taps the device with a finger, causing the LED to light up. This confirms that the mechanical force applied to the ZNW-based device generates sufficient electrical energy to power the LED, demonstrating its real-world applicability in energy harvesting. Figure 6(c) presents the piezoelectric voltage output of ZNWs with different seed layer thicknesses. The piezoelectric output measurements were conducted using a controlled impact test platform (as shown in the inset). A vibration shaker was used to apply a periodic force at a frequency of 1 Hz, exerting a vertical force of 1 N onto the piezoelectric device. The effective active area of the

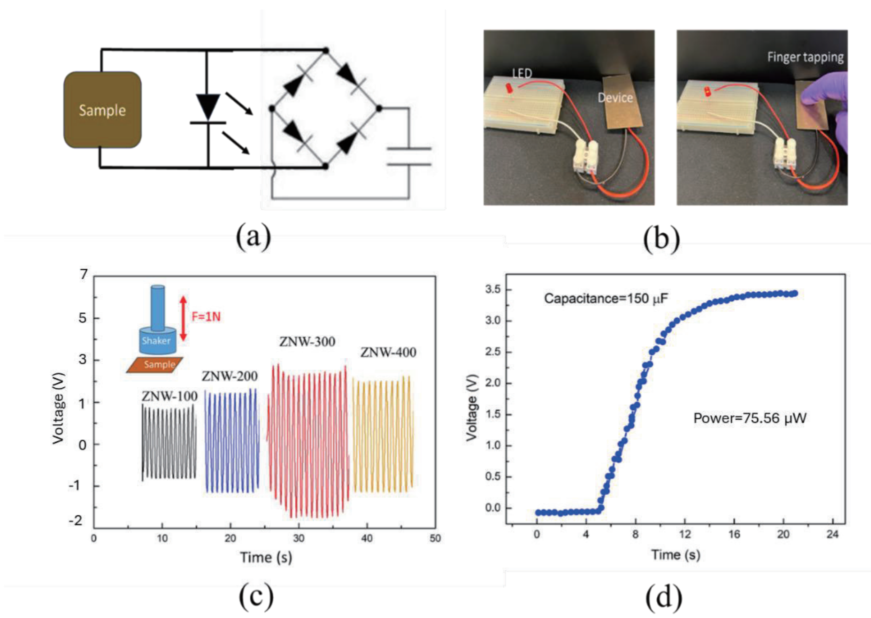

Fig. 6. (Color online) Demonstration of energy harvester and piezoelectric sensor. (a) Schematic of the circuit for energy harvesting and charging. (b) Energy harvesting test; tapping the device with a finger will light up the LED. (c) Voltage output of ZNW-based piezoelectric energy harvester. The inset shows the test setup with an impact force of 1 N. (d) Voltage versus time curve when a 150 μF capacitor is charged by tapping the device with a finger, generating power of about 75.56 μW.

device was 3 × 5 cm^2 (0.0015 m^2). A force sensor was employed to monitor the applied force during the test. The output voltage was recorded using an oscilloscope to analyze the response of the ZNW-based energy harvester under mechanical excitation. The data indicate that ZNW-300 exhibits the highest voltage output, aligning with the earlier findings that ZNWs with a seed layer thickness of 300 nm demonstrate superior piezoelectric performance owing to their optimized aspect ratio and alignment. The measured peak-to-peak voltage outputs for ZNW-100, ZNW-200, ZNW-300, and ZNW-400 were 2, 2.8, 4.6, and 3.3 V, respectively. The increase in voltage output from ZNW-100 to ZNW-300 is attributed to the enhanced aspect ratio and optimized NW growth. In addition, only the seed layer without NW growth (ZSL-400) exhibited a voltage output of only 1.1 V under the same mechanical excitation conditions. This considerable difference in output voltage clearly indicates that the NW architecture plays a crucial role in enhancing the piezoelectric energy harvesting performance. Figure 6(d) shows the voltage–time curve of a 150 μF capacitor being charged by the piezoelectric device when tapped. The voltage steadily increases, reaching about 3.5 V after approximately 12 s of tapping. The generated power P of 75.56 μW from the energy harvester is given by[27]

$$P = \frac{CV^2}{2t}, \tag{2}$$

where C is the capacitance (150 μF), V is the voltage (3.5 V), and t is the charging time (12 s). This confirms the ZNW-based device's potential for sustainable energy harvesting and self-powered applications. The experimental results in Fig. 6 highlight the effectiveness of ZNWs in piezoelectric energy harvesting, demonstrating their ability to convert mechanical energy into usable electrical power. The successful lighting of the LED and the charging of a capacitor emphasize the potential applications of ZNW-based PENGs in wearable electronics, wireless sensor networks, and self-powered systems.

4. Conclusions

In this study, ZNWs with different seed layer thicknesses were successfully synthesized, and their structural characteristics, piezoelectric properties, and energy harvesting performance were systematically analyzed. Experimental results show that ZNW-300 has excellent piezoelectric properties with the highest d_{33} value of 10.5 pm/V. The reason is that ZNW-300 has the highest aspect ratio of 56.55. In addition, the ZNW-300 piezoelectric generator can store energy to charge a 150 μF capacitor to 3.5 V in about 12 s, with a calculated power output of 60.2 μW. This demonstrates the feasibility of utilizing ZNWs for small-scale energy storage and self-powered electronic devices.

Acknowledgments

This work was sponsored by the National Science Council of the Republic of China under the grant No. NSTC 113-2637-E-324-001

References

1 A. Waseem, M. A. Johar, A. Abdullah, I. V. Bagal, J.-S. Ha, J. K. Lee, and S.-W. Ryu: Nano Energy **90** (2021) 106552. https://doi.org/10.1016/j.nanoen.2021.106552

2 G. Liu, Y. Tang, A. M. Soomro, P. Shen, S. Lu, Y. Cai, H. Wang, Q. Yang, H. Chen, Y. Shi, C. Lin, F. Xu, F. Xu, Z. Wu, X. Chen, D. Cai, and J. Kang: Nano Energy **109** (2023) 108265. https://doi.org/10.1016/j.nanoen.2023.108265

3 M. Manrique, V. Consonni, G. Ardila, A. Ghouma, G. L. Rhun, and B. Salem: Nano Trends **9** (2025) 100066. https://doi.org/10.1016/j.nwnano.2024.100066

4 J. Yi, Y. Song, Z. Cao, C. Li, and C. Xiong: Compos. Sci. Technol. **215** (2021) 109011. https://doi.org/10.1016/j.compscitech.2021.109011

5 S. Mishra, P. Supraja, R. R. Kumar, and D. Haranath: Mater. Today: Proc. **102** (2024) 158. https://doi.org/10.1016/j.matpr.2023.04.224

6 R. Damastuti, R. Jayachitra, H. Yu, A. Prasannan, and P.-D. Hong: J. Taiwan Inst. Chem. Eng. **169** (2025) 105957. https://doi.org/10.1016/j.jtice.2025.105957

7 T. Das, S. Tripathy, A. Kumar, and M. Kar: Nano Energy **136** (2025) 110752. https://doi.org/10.1016/j.nanoen.2025.110752.

8 C. X. Wu, T. W. Kim, J. H. Park, B. Koo, S. Y. Sung, J. J. Shao, C. Zhang, and Z. L. Wang: ACS Nano **14** (2020) 1390. https://doi.org/10.1021/acsnano.9b07165

9 Y. S. Tan, K. Yang, B. Wang, H. Li, L. Wang, and C. X. Wang: Nano Res. **14** (2021) 3969. https://10.1007/s12274-021-3322-2

10 T. Yang, H. Pan, G. Tian, B. Zhang, D. Xiong, Y. Gao, C. Yan, X. Chu, N. Chen, S. Zhong, L. Zhang, W. Deng, and W. Yang: Nano Energy **72** (2020) 104706. https://doi.org/10.1016/j.nanoen.2020.104706

11 W. Deng, T. Yang, L. Jin, C. Yan, H. Huang, X. Chu, Z. Wang, D. Xiong, G. Tian, Y. Gao, H. Zhang, and W. Yang: Nano Energy **55** (2019) 516. https://doi.org/10.1039/d4ma00283k

12 S. Taleb, W. M. van Lingen, and M. Acuautla: Mater. Adv. **5** (2024) 7671. https://doi.org/10.1039/d4ma00283k

13 K. Govender, D. S. Boyle, P. B. Kenway, and P. O'Brien: J. Mater. Chem. **14** (2004) 2575

14 L. E. Greene, M. Law, J. Goldberger, F. Kim, J. C. Johnson, Y. Zhang, R. J. Saykally, and P. Yang: Angew. Chem. Int. **42** (2003) 3031. https://doi.org/10.1039/B404784B

15 L. Vayssieres, K. Keis, A. Hagfeldt, and S. Lindquist: Chem. Mater. **13** (2001) 4395. https://doi.org/10.1021/cm011160s

16 B. C. Cheng, Y. H. Xiao, G. S. Wu, and L. D. Zhang: Appl. Phys. Lett. **84** (2004) 416. https://doi.org/10.1063/1.1639131

17 S. K. Sharma and G. J. Exarhos: Solid State Phenom. **55** (1997) 32. https://doi.org/10.4028/www.scientific.net/SSP.55.32

18 J. J. Wu and S. C. Liu: J. Phys. Chem. B **106** (2002) 9546. https://doi.org/10.1021/jp025969j

19 B. Yin, Y. Qiu, H. Zhang, J. Lei, Y. Chang, J. Ji, Y. Luo, Y. Zhao, and L. Hu: Nano Energy **14** (2015) 95. https://doi.org/10.1016/j.nanoen.2015.01.032

20 Z. Shao and X. Li: Physica E **77** (2016) 44. https://doi.org/10.1016/j.physe.2015.11.003.

21 R. S. Sabry and A. D. Hussein: Polym. Test. **79** (2019) 106001. https://doi.org/10.1016/j.polymertesting.2019.106001

22 A. K. Singh, A. Sahu, and P. I. Anand: Nano Trends **9** (2025) 100079. https://doi.org/10.1016/j.nwnano.2025.100079

23 Y. Khazani, E. Rafiee, and A. Samadi: Mater. Chem. Phys. **329** (2025) 130136. https://doi.org/10.1016/j.matchemphys.2024.130136

24 N. J. Tamanna, M. S. Hossain, N. M. Bahadur, and S. Ahmed: Results Chem. **7** (2024) 101313. https://doi.org/10.1016/j.rechem.2024.101313

25 H. Yang, N. Shao, J. Wang, J. Xu, H. Xu, and Y. Zhang: Sustain. Energy Technol. Assess. **73** (2025) 104157. https://doi.org/10.1016/j.seta.2024.104157

26 M. Fortunato, C. R. Chandraiahgari, G. De Bellis, P. Ballirano, P. Soltani, S. Kaciulis, L. Caneve, F. Sarto, and M. S. Sarto: IEEE Trans. Nanotechnol. **17** (2018) 311. https://doi.org/10.1109/TNANO.2018.2800406

27 D. Yang, A. Sun, Y. Pan, and K. Wang: Int. J. Electrochem. Sci. **19** (2024) 100793. https://doi.org/10.1016/j.ijoes.2024.100793